Comparison of RANS, URANS, SAS and IDDES for the prediction of train crosswind characteristics

Xiao-Shuai Huo[1a], Tang-Hong Liu[*1], Zheng-Wei Chen[*2], Wen-Hui Li[1b], Hong-Rui Gao[1c] and Bin Xu[1d]

[1]Key Laboratory of Traffic Safety on Track of Ministry of Education, School of Traffic & Transportation Engineering, Central South University, Changsha 410075, PR China
[2]Department of Civil and Environmental Engineering, The Hong Kong Polytechnic University, Hung Hom, Kowloon, Hong Kong, China

(Received , Revised , Accepted)

Abstract. In this study, two steady RANS turbulence models (*SST k–ω* and Realizable *k–ε*) and four unsteady turbulence models (URANS *SST k–ω* and Realizable *k–ε*, *SST*–SAS, and *SST*–IDDES) are evaluated with respect to their capacity to predict crosswind characteristics on high-speed trains (HSTs). All of the numerical simulations are compared with the wind tunnel values and LES results to ensure the accuracy of each turbulence model. Specifically, the surface pressure distributions, time-averaged aerodynamic coefficients, flow fields, and computational cost are studied to determine the suitability of different models. Results suggest that the predictions of the pressure distributions and aerodynamic forces obtained from the steady and transient RANS models are almost the same. In particular, both SAS and IDDES exhibits similar predictions with wind tunnel test and LES; therefore, the SAS model is considered an attractive alternative for IDDES or LES in the crosswind study of trains. In addition, if the computational cost needs to be significantly reduced, the RANS *SST k–ω* model is shown to provide relatively reasonable results for the surface pressures and aerodynamic forces. As a result, the RANS *SST k–ω* model might be the most appropriate option for the expensive aerodynamic optimizations of trains using machine learning (ML) techniques because it balances solution accuracy and resource consumption.

Keywords: high-speed train; crosswind; RANS; URANS; SAS; IDDES

1. Introduction

Over the past few decades, the number of rail passengers has grown rapidly, making high-speed trains (HSTs) a relatively popular means of transportation compared to cars or airplanes (Niu *et al.* 2017). As HSTs have evolved to be lighter and faster, crosswind stability and operational safety have become extremely important themes (Baker *et al.* 2009; Cheli *et al.* 2012). HSTs caught in

*Corresponding author, Professor, E-mail: lth@csu.edu.cn; Ph.D., E-mail: zhengchen@polyu.edu.hk
[a] Ph.D., E-mail: hxs@csu.edu.cn
[b] Ph.D., E-mail: lwh@csu.edu.cn
[c] Ph.D., E-mail: gaohongrui@csu.edu.cn
[d] Ph.D., E-mail: rb1960637104@gmail.com

crosswinds are often surrounded by complex and irregular turbulent vortices, which greatly increase the risk of overturning and derailing (Krajnović *et al.* 2012; Chen *et al.* 2021). Therefore, it is necessary to study the aerodynamic characteristics of HSTs running under crosswinds.

In general, three different methods, including full-scale measurements (Baker *et al.* 2004; Gao *et al.* 2021), wind tunnel tests (Bocciolone *et al.* 2008; An *et al.* 2020; Li *et al.* 2021), and numerical simulations (Chen *et al.* 2020; Guo *et al.* 2020), are used to assess the crosswind characteristics of HSTs. Compared with the huge difficulties of full-scale measurements and the high costs of wind tunnel tests, numerical simulation is a convenient and economical prediction approach (Huo *et al.* 2020). With the development of the CFD technique, different turbulence models have been successfully employed to deal with the crosswind issues of HSTs, such as aerodynamic loads, pressure distributions, and flow fields (Baker 2010; Zhao *et al.* 2015; Liu *et al.* 2018; Wang *et al.* 2018; Jiang *et al.* 2021).

Currently, the Reynolds-Averaged Navier–Stokes (RANS) is an extensively approved method in engineering applications due to its relatively low computational cost (Catanzaro *et al.* 2010). However, the steady RANS model is inappropriate for the simulation of massively separated flows surrounding trains subjected to crosswinds (García *et al.* 2015). By preserving the transient term, the unsteady RANS (URANS) model could capture the larger-scale turbulent vortices. Large-eddy simulation (LES) is considered to be a reliable method to predict complicated flow structures around HSTs under crosswinds, although its resource consumption is extremely enormous (Hemida and Krajnović 2009). Combining the superiorities of the RANS model and LES, a hybrid model, i.e., detached eddy simulation (DES), was proposed by Spalart and Shur (Spalart and Shur 1997). Meanwhile, DES has been successfully used in the study of train aerodynamic characteristics in crosswinds (Krajnovic 2008; Chen *et al.* 2018). Nevertheless, the inherent drawbacks of the DES model bring challenges to its application, such as modeled-stress depletion (Menter and Kuntz 2004). To overcome these problems, the delayed DES (DDES) model was constructed (Spalart *et al.* 2006), and improved delayed DES (IDDES) model was further developed as a more advanced model (Shur *et al.* 2008). In addition, scale-adaptive simulation (SAS) (Menter and Egorov 2010) has been introduced to deal with a series of problems with train aerodynamics in recent studies. Direct numerical simulation (DNS) is not normally recommended for complex calculations because of its Reynolds number limitation and tremendous computational demands (Morden *et al.* 2015).

Since better solution accuracy is often related to higher computational cost, it is crucial to choose a suitable turbulence model according to the target requirements; that is to say, a compromise needs to be considered to choose a turbulence model. Based on the surface pressures upon a class 43 HST from a wind tunnel test for a 0° yaw angle, Morden et al. (Morden *et al.* 2015) compared the predictions of five RANS models and two DES methods with experimental data. They found that the DDES method could better reproduce the results of the wind tunnel test. Wang et al. (Wang *et al.* 2017) adopted three unsteady turbulence models to evaluate their performances in terms of predicting the slipstream induced by a HST. Their results indicated that SAS might be an appropriate alternative for IDDES because the SAS model attained a similar degree of precision with less computational expense. Munoz-Paniagua et al. (Munoz-Paniagua *et al.* 2017) compared the performances of different turbulence models for the simulation of crosswind characteristics for a HST, and they concluded that the Explicit Algebraic Reynolds Stress Model (EARSM) could provide relatively reasonable results with consideration of both the computational consumption and the solution accuracy. To choose an appropriate turbulence model, Li et al. (Li *et al.* 2019) conducted six different RANS models to determine the aerodynamic behaviors of an ICE2 model under crosswinds. Compared to wind-tunnel data, the Shear Stress Transport (*SST*) k–ω model exhibited

better prediction results for the lateral and lift forces than other models. In addition, Maleki et al. (Maleki *et al.* 2017) assessed the ability of RANS, URANS, SAS, and ELES to predict the flow field and forces on a double-stacked freight wagon at a 0° yaw angle. Their results revealed that the SAS presented predictions that were highly similar to those of ELES and a wind tunnel test, though a RANS model might have been an attractive approach if only the pressure drag was needed.

Based on the above analysis, the various turbulence models have different effects on the prediction of train aerodynamic performance. However, under crosswinds, a systematic comparison of the capacity of steady RANS, URANS, and more advanced hybrid models to predict flow field characteristics and the aerodynamic forces on a train has not been conducted. Therefore, in this study, two steady RANS models, *SST* k–ω and Realizable k–ε, and four unsteady models, URANS *SST* k–ω and Realizable k–ε, *SST*–SAS, and *SST*–IDDES, were proposed to evaluate their prediction accuracy in terms of the pressure distributions, aerodynamic forces, and flow fields. The wind tunnel data collected by Copley (Copley 1987) were introduced for comparison to estimate the fidelity of all models. Specifically, there were two main research objectives of this study. First, the influence mechanisms of different turbulence models on the train aerodynamic characteristics subjected to crosswinds were studied. Second, an economical and accurate turbulence model was necessary for the aerodynamic optimizations of trains using machine learning (ML) techniques. For example, Munoz-Paniagua and García (Muñoz-Paniagua and García 2019) adopted genetic algorithms (GAs) to optimize a train nose in two different scenarios, and a large number of computational cases were performed to meet the requirements of a metamodel. Thus, the solution accuracies and the resource consumption of all turbulence models used in this study for aerodynamic responses were compared to determine a suitable turbulence model for the aerodynamic optimizations of trains in future work.

This paper is constructed as follows. The numerical details, including the train model, computational domain, boundary conditions, mesh generation, and descriptions of the turbulence models, are presented in Section 2. In Section 3, the effect of the grid resolution is discussed. Then, the study of the pressure distributions, aerodynamic forces, flow fields, and computational cost is described. Finally, conclusions are summarized in Section 4.

2. Numerical details

2.1 Computational domain and boundary conditions

In this study, an idealized train model described by Chiu and Squire (Chiu and Squire 1992) was adopted to investigate the performance of different turbulence models for predicting the flow under crosswind. As demonstrated in Fig. 1(a), the dimensions of this idealized train model were 10 D × D × D (D was a characteristic size equal to 125 mm), and its cross-sectional profile was defined as follows:

$$|y|^n + |z|^n = c^n \tag{1}$$

The train was formed by a nose and a train body. The train body was a cylindrical uniform section, and c and n in Eq. (1) were 62.5 mm (D/2) and 5, respectively. Towards the nose cross-section, c followed a semi-elliptical profile with a major diameter of 1.28 D in the same equation, and n decreased uniformly from 5 to 2 at the tip of the nose. Thus, the cross-section gradually formed a circle.

The configuration and domain of the model are displayed in Fig. 1(b). Referring to the wind

tunnel tests conducted by Copley (Copley 1987), the train was mounted on the side wall of the computational domain, which was similar to the LES simulation performed by Hemida and Krajnović (Hemida and Krajnović 2010). The dimensions of the hexahedral computational domain were 48.19 *D* (length), 15.74 *D* (width), and 10 *D* (height). The train model was yawed 35° to the direction of incoming flow and positioned 10 *D* downstream of the inlet and 30 *D* upstream of the outlet. The coordinate system was aligned with the train direction, and the original point of the coordinate axes was defined as the nose tip.

In the wind tunnel tests (Copley 1987), a ground board was used to control the boundary layer development, as shown in Fig. 1(c). In our simulations, the ground condition was modeled simply by setting the bottom of the computational domain to be at the height of the test floor. The clearance between the ground and the train was set to 0.15 *D*, which was consistent with the experimental setup. In addition, two identical models (one model was a mirror image of the other) were installed on either side of the ground board to simulate the relative movement between the train and the floor in the tests, which was different from our simulation configuration.

A constant freestream velocity condition was employed in the inlet boundary. Based on the train height (*D*) and the inflow velocity (U_f), the Reynolds number was 3.7×10^5, matching the wind tunnel test. The outlet boundary corresponded to a zero static pressure condition. No-slip wall conditions were imposed at all train surfaces, ground, top, and side walls of the domain.

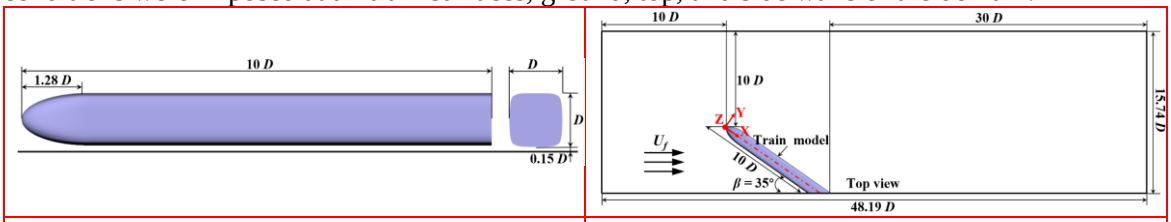

(a) Train model (b) Computational domain

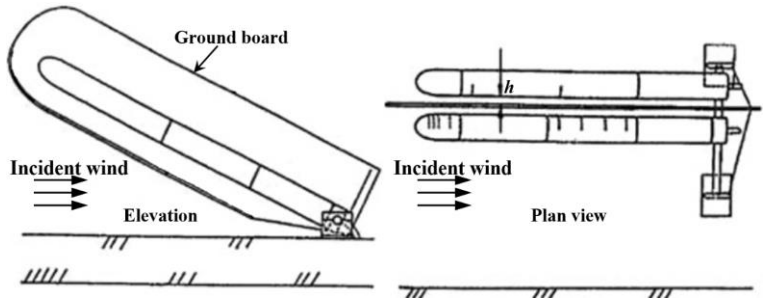

(c) Wind tunnel model of Copley (Copley 1987)

Fig. 1 Model configuration

2.2 Meshing strategy

The hexahedral grids were constructed with SnappyHexMesh in the OpenFOAM mesh generator package in all of the simulations. According to the identical meshing strategy, three different grid densities—coarse, medium, and fine grids—were generated for grid independence verification. The total number of cells was approximately 8 million, 15 million, and 26 million for the coarse grid, medium grid, and fine grid, respectively. Two different levels of refinement boxes were used to accurately capture the turbulent vortices surrounding the train, as shown in Fig. 2(a). The dimensions

of the two refinement boxes were approximately 35.0 D × 9.5 D × 2.5 D (extra-fine refinement box) and 35.0 D × 20.5 D × 5.0 D (fine refinement box). In addition, a smooth transition was conducted at the interface of the two refinement boxes. Fig. 2(b) exhibits a three-dimensional view of the train surface mesh. Inflation layers were imposed at all of the walls to better simulate the boundary layer development, as presented in Fig. 2(c). As the grid became finer, the cell size of the train surface and the two refinement boxes was gradually reduced, while the number of corresponding inflation layers on all of the walls was increased. Details of the three grid resolutions are presented in Table 1. Moreover, the enhanced wall treatment (EWT) was adopted for the ε-equation, and a y^+-insensitive wall treatment was applied in the ω-equation to appropriately determine the shear stress in the first cell near the wall.

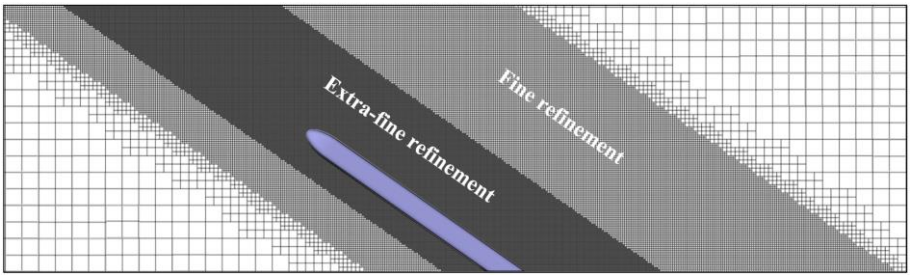

(a) Top view of the grid for the computational domain

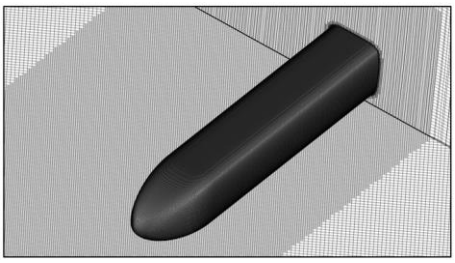

(b) Grid on the train surface

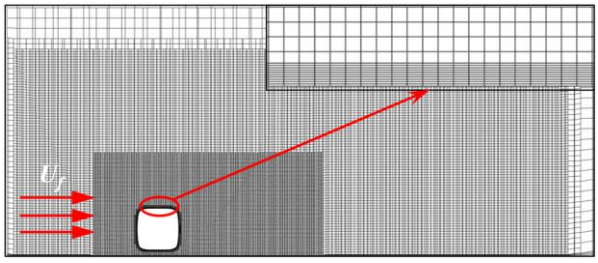

(c) Grid on a cross-sectional plane

Fig. 2 Medium grid

Table 1 Details of the different grid resolutions

Grids	Coarse	Medium	Fine
Number of cells	8 million	15 million	26 million
Number of inflation layers	8	10	12
Size of train surface mesh	0.009 D–0.024 D	0.006 D–0.015 D	0.003 D–0.009 D
Grid size in extra-fine refinement box	0.036 D–0.054 D	0.024 D–0.042 D	0.018 D–0.036 D
Grid size in fine refinement box	0.054 D–0.072 D	0.042 D–0.064 D	0.036 D–0.054 D
Train surface wall y^+	10–40	5–20	1–10

2.3 Numerical method

Two steady RANS turbulence models (*SST* k–ω and Realizable k–ε) and four unsteady turbulence models (URANS *SST* k–ω and Realizable k–ε, *SST*–SAS, and *SST*–IDDES) were considered in this

study. For the time-averaged simulations, no detailed description is provided here due to their popularity and the fact that these types of simulations are already well-established (Cheli *et al.* 2010; Li *et al.* 2019). Only the instantaneous turbulence models (URANS, SAS, and IDDES) are introduced in the subsequent content.

2.3.1 URANS

In the Reynolds averaging method, the variables to be resolved were decomposed into the mean component and the fluctuating component in the transient Navier-Stokes (N-S) equations (ANSYS 2013). As common RANS equations, URANS equations preserved the instantaneous term. For the incompressible flow, the URANS equation could be written as:

$$\frac{\partial \overline{u}_i}{\partial x_i} = 0 \tag{2}$$

$$\frac{\partial \overline{u}_i}{\partial t} + \frac{\partial \overline{u}_i \overline{u}_j}{\partial x_j} = -\frac{1}{\rho}\frac{\partial \overline{p}}{\partial x_i} + \upsilon \frac{\partial^2 \overline{u}_i}{\partial x_j \partial x_j} - \frac{\partial \overline{u_i' u_j'}}{\partial x_j} \tag{3}$$

where the dependent variables such as the velocity term (u) or pressure term (p) are a function of both the spatial coordinates (x) and the time (t), the bar and the prime denote the mean and fluctuating components, respectively, and ρ is the fluid density.

It should be noted that $\overline{u_i' u_j'}$ appeared on the right side of Eq. (3), which was the Reynolds stress tensor term due to fluctuating velocities, and this could not be formally expressed. To close the above equations, different turbulence models were applied to approximate the Reynolds stress according to the mean velocity gradient and the spatially varying eddy viscosity. Thus, two further equations were proposed to solve these problems, such as the well-known k–ε model. In addition, more forms of two-equation eddy-viscosity models were established, such as the k–ω and *SST* k–ω models. Combined with the classical k–ω with k–ε models, the *SST* k–ω was a hybrid model that blended k–ω modeling of near-wall boundaries with k–ε in the further flow (Menter 1994). The Realizable k–ε model could provide the optimal performance of all the k–ε model versions for separated flows and flows with complex secondary flow features (ANSYS 2013). As a result, the *SST* k–ω and Realizable k–ε models were selected for comparison.

2.3.2 SAS

SAS is an improved URANS model that can solve for large-scale motions and the turbulent spectrum under unsteady flow conditions (ANSYS 2013). In the SAS model, the von Kármán length scale was implemented to predict the scale-adaptive temporal and spatial scales. In addition, the *SST*–SAS model was proposed by Menter and Egorov (Menter and Egorov 2010), which blended the SAS features with the k–ω *SST* model. In recent years, the *SST*–SAS model has been gradually improved and embedded in ANSYS FLUENT (ANSYS 2013). The von Kármán length scale employed in the *SST*–SAS is given by:

$$L_{vK} = \kappa \left| \frac{\overline{U}'}{\overline{U}''} \right| \tag{4}$$

where $\bar{U}'$ is the first velocity derivative $\sqrt{2S_{ij}S_{ij}}$; $S_{ij}=\frac{1}{2}\left(\frac{\partial \bar{u}_i}{\partial x_j}+\frac{\partial \bar{u}_j}{\partial x_i}\right)$, and $\bar{U}''$ is the second velocity derivative $\sqrt{\frac{\partial^2 \bar{u}_i}{\partial x_j \partial x_j}\frac{\partial^2 \bar{u}_i}{\partial x_k \partial x_k}}$. Readers can find more detailed descriptions about the *SST*–SAS model in Menter and Egorov (Menter and Egorov 2010).

As a scale-adaptive method, the SAS model could automatically adjust to resolved structures in the URANS simulations in terms of the von Kármán length scale. Additionally, this model provided standard RANS abilities in steady flow regions. In the *SST*–SAS model, an additional SAS-term (Q_{SAS}) in the ω-equation dynamically switched itself on when the flow was sufficiently unstable (Davidson 2006). Therefore, this SAS-term decreased the turbulent viscosity when unsteadiness was detected, which led to LES-type behavior in the unstable flow regions.

2.3.3 IDDES

DES, as a mix of LES and RANS, was designed to reduce the cost of LES while still retaining accuracy and reliability. The near-wall boundary-layer region was treated with RANS, and the further separated vortices were captured with LES (Spalart and Shur 1997). However, modeled-stress depletion (MSD) and grid-induced separation (GIS) are two obvious drawbacks of the common DES (Menter and Kuntz 2004). To provide shielding against the above issues, the IDDES model was presented by Shur et al. (Shur *et al.* 2008), similar to the DDES model (Spalart *et al.* 2006). Thus, the *SST*–IDDES model was used in this study. This model employed an improved delayed shielding function to obtain higher accuracy at the interface of the RANS/LES region and to enhance the wall-modeling capability.

In the IDDES model, an alternative and new definition of the subgrid length scale was written as:

$$\Delta=\min\left\{\max\left[C_w d_w, C_w h_{\max}, h_{wn}\right], h_{\max}\right\} \tag{5}$$

where C_w denotes an empirical constant of 0.15 (Shur *et al.* 2008), d_w is the distance to the wall, h_{wn} is the grid step in the wall-normal direction, and $h_{\max}=\max\left\{h_x, h_y, h_z\right\}$ represents the largest local grid spacing. A fuller description of IDDES can be seen in Shur et al. (Shur *et al.* 2008).

2.3.4 Numerical setup

The CFD code ANSYS FLUENT 18.1 was utilized to simulate all the computations. In all simulations, the SIMPLEC scheme was selected for the pressure and velocity coupling. For the spatial discretization methods of the RANS simulations, the second-order upwind scheme was adopted for the pressure and momentum equations. For the SAS and IDDES, the bounded central differencing scheme was selected for the momentum equation, and the Least Square Method was used to solve the gradients. In addition, the turbulent kinetic energy and the turbulent dissipation rate were set to the second-order upwind scheme. The bounded second-order implicit scheme was applied in the transient terms. For the whole process of unsteady simulations, a fixed time step of 5×10^{-5} s was applied to guarantee a mean Courant-Friedrichs-Lewy (CFL) number of approximately 1.0. In addition, thirty iterations per time step were adopted as the maximum number, and the residual of each equation was no more than 10^{-5} to meet the requirements of convergence criterion.

For convenient comparison, the side force (F_s), lift force (F_l), and pressure (P) were converted into non-dimensional coefficients, as follows:

$$C_s = \frac{F_s}{0.5\rho U_f^2 S_y} \tag{6}$$

$$C_l = \frac{F_l}{0.5\rho U_f^2 S_z} \tag{7}$$

$$C_p = \frac{P - P_0}{0.5\rho U_f^2} \tag{8}$$

where C_s, C_l, and C_p are the side force, lift force, and pressure coefficients, respectively; ρ is the air density at standard atmospheric pressure; U_f is the freestream speed; S_y and S_z are the projected areas in the y and z directions, respectively; and the reference pressure P_0 is considered to be the pressure at infinity.

3. Results and discussion

3.1 Effect of grid resolution

To investigate the effect of grid resolution, three grids with different densities were constructed for comparison, as described in Section 2.2. The URANS Realizable k–ε and IDDES turbulence models were chosen to perform the grid independence analysis. The time-averaged C_s and C_l of the train from the different grid densities are presented in Table 2. According to the results of the two turbulence models, the aerodynamic coefficients of the medium and fine grids showed better consistency, while shifting to the coarse grid had an obvious effect on C_s and C_l. In addition, the maximum errors of C_l between the coarse and fine grids with respect to the URANS k–ε and IDDES models were 10.94% and 7.73%, respectively. The time-averaged pressure profiles for two cross-sections are illustrated in Fig. 3. The results of all the numerical simulations indicated a qualitative consistency with the experimental values obtained from Copley (Copley 1987). Similarly, the pressure distributions of the medium grid agreed well with those of the fine grid for the two models. However, the difference between the coarse grid and the remaining two grids was not negligible, especially on the leeward side (LWS) and the bottom. The discrepancy between our simulations and the wind tunnel data is explicitly discussed in the subsequent content. In terms of the above analysis, the strategy of the medium grid was sufficient to evaluate different turbulence models, and so the following analysis was based on the medium grid in this study.

Table 2 Time-averaged C_s and C_l for the different grid resolutions

Items	URANS k–ε				IDDES		
	Coarse	Medium	Fine		Coarse	Medium	Fine
C_s	0.531	0.579	0.583		0.604	0.639	0.646
C_l	0.342	0.380	0.384		0.394	0.421	0.427

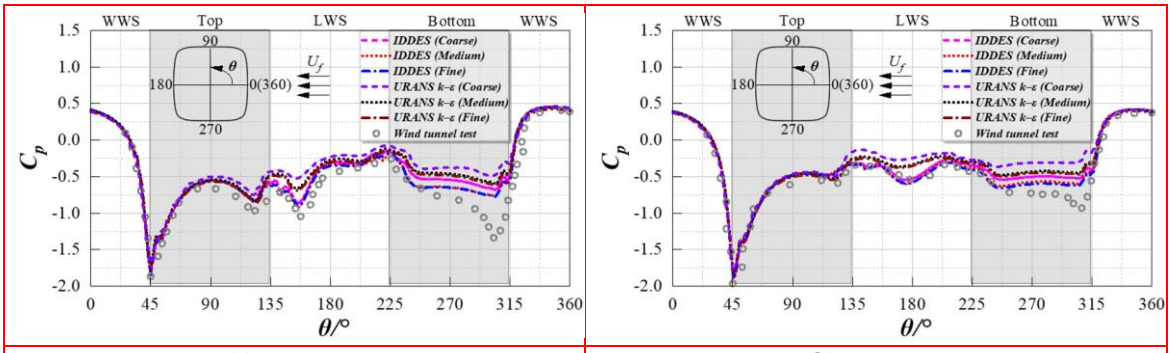

(a) x/D = 2.5 (b) x/D = 4.5

Fig. 3 Comparison of the time-averaged surface pressure coefficients for different grid resolutions at two distances from the nose tip

3.2 Pressure distributions and aerodynamic forces

The time-averaged pressure distributions for three cross-sections that were obtained with our numerical simulations were compared with those of the wind tunnel test (Copley 1987), as presented in Fig. 4. The LES simulation reported by Hemida and Krajnović (Hemida and Krajnović 2010) is also plotted in Fig. 4 for further comparison. Only one cross-section (x/D = 6.5) was found in their study. In total, all of the numerical models predicted similar pressure distributions and reflected the approximate tendency of the experimental data. The pressure coefficients on the bottom of the train were significantly overestimated for all of the models. This discrepancy might have occurred because the ground configuration in the simulations was different from that in the test. Two of the same models were symmetrically installed on either side of the ground board in the test, while only one model was mounted on the side wall in the numerical simulations. Thus, a stagnation area was formed between the train and the side wall. This stagnation area led to a greater increase in the pressure on the streamwise face than that for the wind tunnel test. In addition, smaller differences were found in the section x/D = 4.5 (away from the nose and tail of the train), where the vortex structures were relatively stable.

For either of the two RANS models, the pressure distributions predicted by the steady and unsteady methods were extremely similar. This phenomenon meant that increasing the transient term in the RANS equations had little effect on the prediction of the pressure distribution. In particular, the Realizable k–ε model overpredicted the pressure coefficients on the LWS and the bottom compared to the experimental value, which was related to the poor performance of Realizable k–ε in predicting complex flows near the wall. However, the RANS/URANS *SST* k–ω model provided a closer pressure prediction compared to the other turbulence models, although slight differences could be observed on the LWS. It could be found that the SAS and IDDES models exhibited similar pressure predictions on all cross-sections. In addition, the discrepancies of the LES relative to both the SAS and IDDES were only observed at the upper half of the LWS (θ from 135° to 180°) in Fig. 4(c). The good agreement of our numerical simulations with the LES results and the wind tunnel data was greatly encouraging, although there was an overestimation of the pressure coefficients at the bottom.

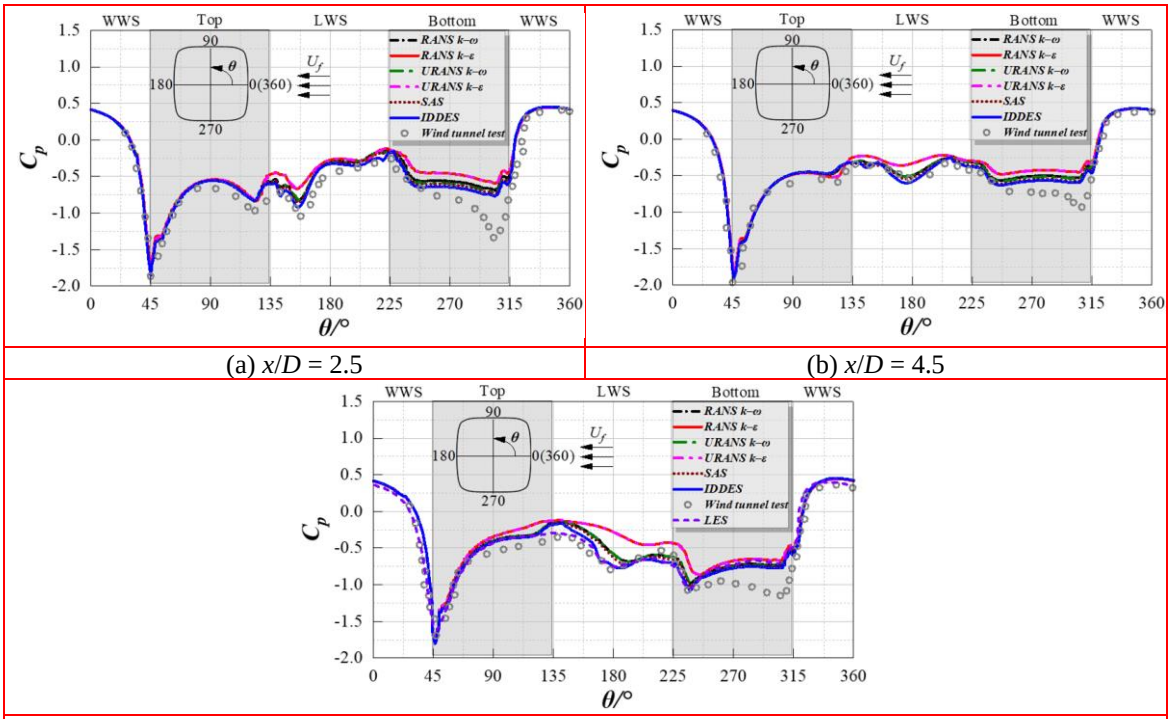

(a) x/D = 2.5

(b) x/D = 4.5

(c) x/D = 6.5

Fig. 4 Surface pressure distributions on three cross-sections (The experimental data were obtained from Copley (Copley 1987))

In general, the crosswind stability of a train is widely analyzed based on the side force or the lift force. Due to the lack of experimental aerodynamic force coefficients, the time-averaged C_s and C_l predicted by different turbulence models in this study were compared with that of LES (Hemida and Krajnović 2010) in Table 3. All of the models had different degrees of underestimation of aerodynamic force coefficients compared to the LES values, which could be well explained, as illustrated in Fig. 4. The IDDES provided better results, which were within 2% of the LES data. The predictions of the SAS were very close to those of the IDDES. In addition, the *SST k–ω* showed better performance in predicting the aerodynamic coefficients than Realizable *k–ε* for the RANS or URANS methods. Moreover, for the *SST k–ω* model, the maximum difference in the time-averaged force coefficients was lower than 5% compared to the LES, while the differences in C_s and C_l for the Realizable *k–ε* model and the LES were up to 10.75% and 12.51%, respectively. As a result, IDDES could be considered to be the turbulence model that provided the closest predictions to the LES and wind tunnel data, although the (U) RANS *SST k–ω* model was probably a preferable model due to its lower cost and relatively similar results.

Table 3 Time-averaged C_s and C_l for the different turbulence models

Cases	C_s	C_l	Difference (C_s/C_l)
LES (Hemida and Krajnović 2010)	0.646	0.430	–
RANS *k–ω*	0.614	0.409	4.92%/4.89%
RANS *k–ε*	0.577	0.376	10.75%/12.51%

URANS k–ω	0.619	0.411	4.18%/4.36%
URANS k–ε	0.579	0.380	10.37%/11.72%
SAS	0.631	0.417	2.28%/3.02%
IDDES	0.639	0.422	1.04%/1.86%

3.3 Analysis of flow field

According to the aforementioned analysis of the pressure distributions and aerodynamic forces in Section 3.2, the predictions obtained with the steady and transient RANS models were almost the same, whether or not the Realizable k–ε or *SST* k–ω was adopted. Thus, four instantaneous turbulence models were chosen for the further analysis of the flow structures.

The time-averaged flow patterns, in terms of the streamlines projected on the train surfaces, were demonstrated in Fig. 5. All of the surfaces were rendered by the time-averaged pressure coefficients. On the windward side (WWS) of the train, one attachment line was identified at the middle position in Fig. 5(a), and we did not find obvious differences in the flow patterns or pressure distributions for all models. The flow stretched towards the top and bottom of the train due to this attachment line driving. More complex flow patterns can be identified on the LWS in Fig. 5(b). The separation and attachment lines were evidently captured by the IDDES, SAS, and URANS *SST* k–ω, while relatively smooth flow appeared on the surface for the URANS Realizable k–ε. It was difficult to distinguish the apparent differences between the IDDES and the SAS, although slight discrepancies occurred on the LWS surface of the rear half. The URANS *SST* k–ω presented a similar pattern compared to the IDDES or the SAS. In addition, the separation line, S_1, and the attachment line, A_1, downstream of the train for the URANS *SST* k–ω were closer to the bottom than those of the IDDES or the SAS. However, no obvious bifurcation lines were observed at the rear part for the URANS Realizable k–ε. The streamlines were attached almost entirely to the top surface of the train, and the flow separation emerged at the corner between the top and LWS, as illustrated in Fig. 5(c). Moreover, compared with the URANS Realizable k–ε, the earlier flow separation at the upper leeward edge in region *M* was identified for the URANS *SST* k–ω, SAS, and IDDES models. As the flow moved towards the train end, a recirculation bubble was formed. The SAS displayed an extremely similar bubble to the IDDES. For the URANS models, the bubble for the *SST* k–ω slightly shifted toward the LWS, while the Realizable k–ε showed a larger bubble that was closer to the LWS compared to the IDDES and the SAS. Additionally, a similar phenomenon was observed at the bottom surface, as shown in Fig. 5(d). A separation line was found at the lower leeward edge, and the URANS Realizable k–ε exhibited a shorter separation line in region *N* compared to the remaining models. Furthermore, an insufficiently formed separation bubble was recognized at the train tail for the IDDES, SAS and URANS *SST* k–ω, while a smoother flow was completely attached to the bottom face for the URANS Realizable k–ε.

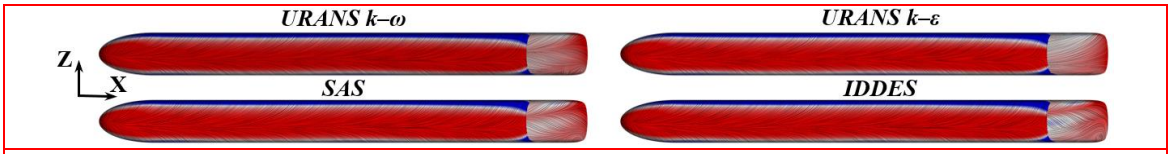

(a) WWS

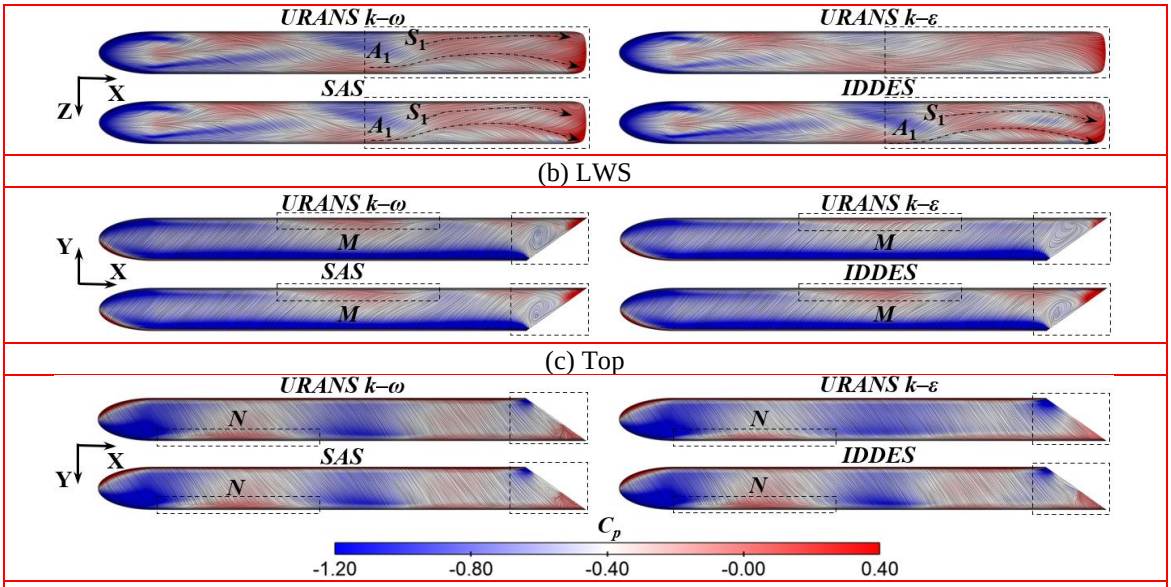

Fig. 5 Time-averaged streamlines on train surface in different views

Based on the time-averaged velocity streamlines projected on six cross-sections, Fig. 6 shows the evolution of the primary vortices. A pair of upper and lower vortices (V_1 and V_2) were separated from the train nose. Vortex V_1 was basically attached on the train surface, and it detached from the LWS face until x/D = 5.5. Vortex V_2 developed backwards and away from the train body. Vortices V_1 and V_2 both gradually grew in size and dissipated in the wake. The flow at the bottom shed a series of vortices, including vortices V_3 and V_5. At the same time, vortex V_4 originated from the upper leeside edge. Finally, all of these vortices were separated from the surface of the train and were subsequently convected downstream in the wake. Similar phenomena can be observed in Hemida and Krajnović (Hemida and Krajnović 2010) for the development of flow structures.

No significant discrepancies were recognized in the first two cross-sections (x/D = 1.5 and 2.5) for the four turbulence models. At x/D = 3.5, similar developments of vortices V_1–V_4 were observed for the IDDES, SAS, and URANS *SST k–ω*, while the URANS Realizable *k–ε* showed a lower intensity of V_2 and insufficient detachment of V_3 and V_4. As Vortex V_2 moved backwards along the train, it almost disappeared at x/D = 4.5 for the URANS Realizable *k–ε*. Additionally, the URANS *SST k–ω* presented an incomplete recirculation region of Vortex V_2, while a similar evolution of Vortex V_2 was detected for the IDDES and SAS. For Vortex V_1, no obvious difference was found among the URANS *SST k–ω*, SAS, or IDDES models, while the intensity of the URANS Realizable *k–ε* was lower at x/D = 4.5–6.5. Vortex V_5 was generated near the ground at the section x/D = 5.5, and Vortex V_3 stretched from the bottom edge of the LWS towards the middle of the train. The intensity of Vortex V_3 for the URANS Realizable *k–ε* was higher than that for the IDDES, SAS, and URANS *SST k–ω* at x/D = 6.5, which directly affected the pressure distribution on the train surface, as shown in Fig. 4(c). Moreover, Vortex V_5 moved upwards and gradually merged with Vortex V_1, as traced from x/D = 5.5 to x/D = 6.5 for the IDDES, SAS, and URANS *SST k–ω* compared to the URANS Realizable *k–ε*. Additionally, the lower intensity of Vortex V_5 was identified for the URANS Realizable *k–ε* relative to the other models.

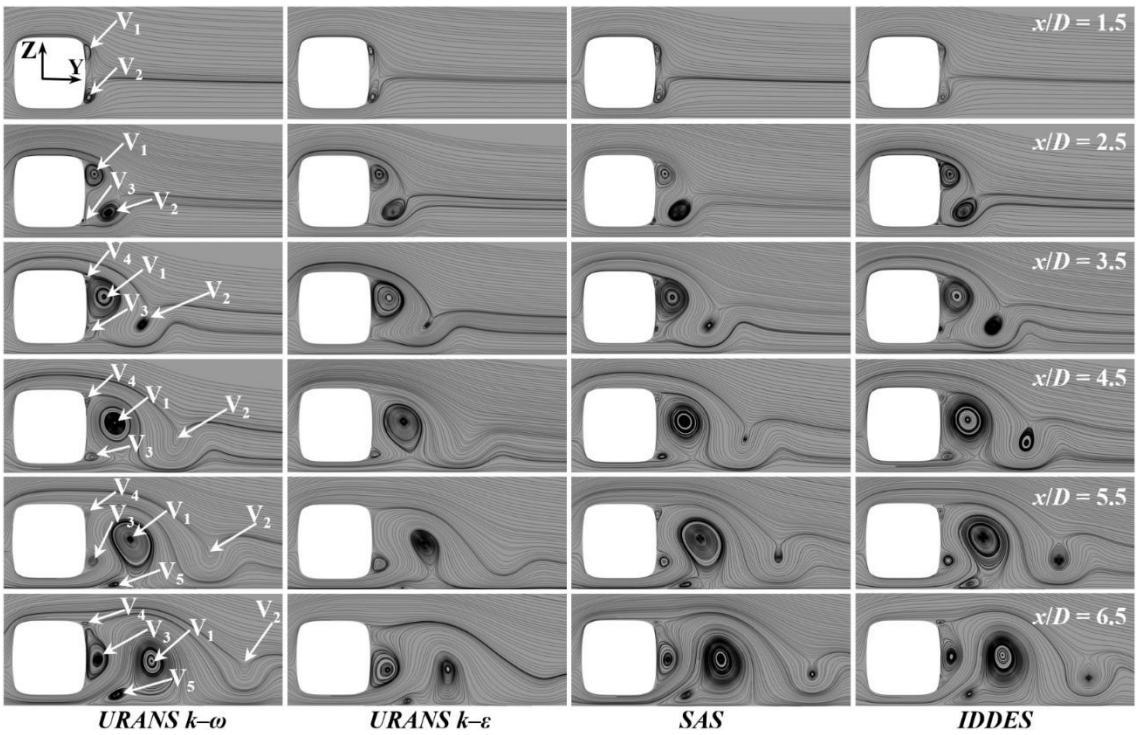

Fig. 6 Time-averaged velocity streamlines projected on *y*-*z* planes at distances of x/D = 1.5, 2.5, 3.5, 4.5, 5.5, and 6.5 to the nose tip

The instantaneous coherent structures of the flow field are illustrated in Fig. 7. The flow structures were identified in terms of the iso-surface of the second invariant, the Q-criterion (Q = 50,000). In addition, all of the iso-surfaces were rendered by the non-dimensional velocity magnitude (U/U_f). This method of identifying vortices was extensively used in the transient flow. In total, the vortices on the upper half of the train body were relatively coherent and smooth, while massive unsteady eddies were shed in the wake flow after x/D = 6. Furthermore, the cores of these vortices gradually extended backwards parallel to the ground. Significant differences were observed between the URANS models that displayed smoother vortices and the hybrid models that presented more complicated flow structures. For the URANS models, *SST* k–ω provided a relatively larger range of vortex structures on the LWS than Realizable k–ε did, although further and smaller vortices were still not captured. The inadequacy of URANS for predicting substantial separation eddies is well known, and this was consistent with other studies. The SAS revealed a similar resolution of the turbulent vortex structures to the IDDES, while smaller structures near the wake were only successfully detected by the IDDES. This result indicated that the dissipation of the inhibiting instability in the momentum equation was greater for the SAS compared to IDDES. Nevertheless, it was encouraging that the SAS could provide highly similar predictions to the IDDES, because the SAS allowed the LES–type behavior to occur due to the von Kármán length scale, thereby resulting in the large turbulent scales and the exact part of the turbulence spectrum being resolved.

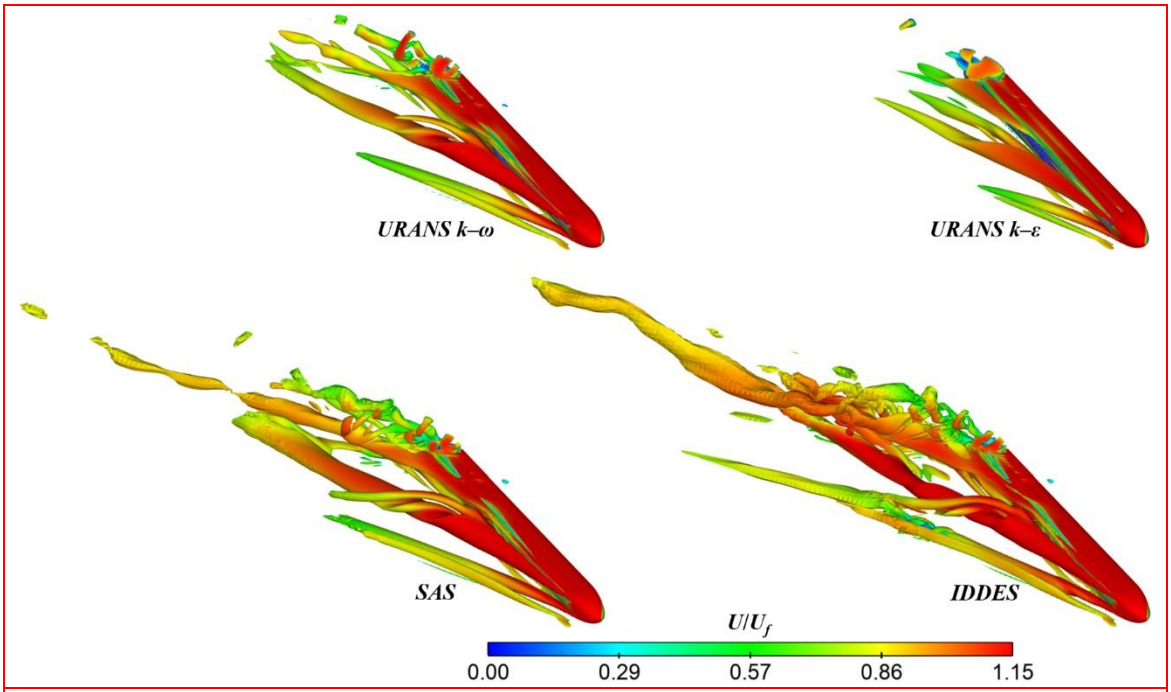

Fig. 7 Iso-surface of the second invariant (Q = 50,000) colored by the normalized velocity magnitude

3.4 Computational cost

In general, the computational cost is a critical parameter for engineering problems when choosing a turbulence model. All numerical simulations in this study were performed at the National Supercomputing Center in Wuxi, China, running on 96 central processing units (CPUs) in parallel. The number of iterations and the CPU time for each model are presented in Table 4. For the sake of comparison, the computational time of RANS *SST k–ω* was selected as the benchmark. Hence, the relative costs of all models in comparison to RANS *SST k–ω* are listed in Table 4. As expected, the steady simulations required much less time to satisfy the convergence criteria than the unsteady simulations. Although the RANS Realizable *k–ε* had the lowest cost, its poor accuracy was not preferred. In fact, the RANS *SST k–ω* might be a good choice for engineering applications if the main concern is only aerodynamic forces due to its lower cost and relatively reasonable accuracy. In addition, it was of great significance to better understand the development of flow fields around a train under crosswinds. It was worth noting that the SAS provided similar flow predictions as the IDDES, which made the SAS a very attractive method. In other words, the SAS was a compromise between the computational cost and the solution accuracy for the flow structures because the cost of SAS was approximately 33.36% lower than that of IDDES. Not surprisingly, the RANS feature of SAS saved computational time.

Table 4 Comparison of computational costs for different turbulence models

Models	Number of iterations	CPU time (s)	Difference (%)
RANS *k–ω*	10,000	20,160	1

RANS k–ε	10,000	16,935	0.84
URANS k–ω	176,000	269,942	13.39
URANS k–ε	176,000	253,210	12.56
SAS	244,000	490,089	24.31
IDDES	244,000	735,438	36.48

4. Conclusions

In this study, numerical simulations based on two steady RANS turbulence models and four unsteady turbulence models were conducted to evaluate the capability of each model to predict crosswind characteristics on trains. The wind-tunnel data and LES results were introduced for comparison with our numerical predictions. In addition, the effect of grid resolution was analyzed in terms of the URANS Realizable k–ε and IDDES models with three different densities.

Although all of the numerical simulations presented a qualitatively good agreement with the experimental data, small deviations appeared at the bottom of the train due to the influence of the boundary layer thickness. The RANS Realizable k–ε model overpredicted the pressure coefficients for the LWS and the bottom, leading to 10.75% and 12.51% differences in C_s and C_l compared with the LES values, while the differences in C_s and C_l between the RANS *SST* k–ω model and the LES were within 5%. Additionally, the surface pressure distributions and the aerodynamic forces predicted by the steady and instantaneous RANS models were almost identical, regardless of whether the *SST* k–ω or Realizable k–ε model was used.

The SAS and IDDES methods provided more precise results than RANS/URANS *SST* k–ω and Realizable k–ε, with respect to the pressure and force coefficients. Moreover, no notable differences in the time-averaged or instantaneous flow patterns were observed between the IDDES and the SAS. However, the URANS approaches failed to predict substantial flow separations or small-scale vortices. In particular, the URANS Realizable k–ε showed a smoother flow pattern and a smaller range of wake vortices than the other models.

In total, the SAS is a very attractive alternative to IDDES or LES in the crosswind study of HSTs due to its relatively lower cost. In addition, a significant reduction of the computational cost was found for the RANS *SST* k–ω model, which could provide relatively reasonable results for surface pressures and aerodynamic forces. Therefore, the RANS *SST* k–ω model is recommended as the most suitable option for the expensive aerodynamic optimizations of trains using ML techniques because it balances solution accuracy and resource consumption.

Acknowledgments

This work was supported by the National Key R&D Program of China (Grant No. 2020YFA0710903) and the Fundamental Research Funds for the Central Universities of Central South University (Grant No. 2021zzts0171).

References

An, J.D., Wang, T.T., Shi, Y.F., Wu, X.X., Liu, Y.Y., Huo, J.Z. and Ding, B. (2020), "A multi-responsive regenerable water-stable two-dimensional cadmium (II) fluorescent probe for highly selective, sensitive and real-time sensing of nitrofurazone and cupric ion", *J Mol Struct*. **1216**. https://doi.org/10.1016/j.molstruc.2020.128328.

ANSYS, I. (2013), *Ansys fluent theory guide*, Cannonsburg, PA, USA: ANSYS, Inc

Baker, C. (2010), "The simulation of unsteady aerodynamic cross wind forces on trains", *Journal of wind engineering and industrial aerodynamics*. **98**(2), 88-99. https://doi.org/10.1016/j.jweia.2009.09.006.

Baker, C., Cheli, F., Orellano, A., Paradot, N., Proppe, C. and Rocchi, D. (2009), "Cross-wind effects on road and rail vehicles", *Vehicle system dynamics*. **47**(8), 983-1022. https://doi.org/10.1080/00423110903078794.

Baker, C., Jones, J., Lopez-Calleja, F. and Munday, J. (2004), "Measurements of the cross wind forces on trains", *Journal of Wind Engineering and Industrial Aerodynamics*. **92**(7-8), 547-563. https://doi.org/10.1016/j.jweia.2004.03.002.

Bocciolone, M., Cheli, F., Corradi, R., Muggiasca, S. and Tomasini, G. (2008), "Crosswind action on rail vehicles: Wind tunnel experimental analyses", *Journal of wind engineering and industrial aerodynamics*. **96**(5), 584-610. https://doi.org/10.1016/j.jweia.2008.02.030.

Catanzaro, C., Cheli, F., Rocchi, D., Schito, P. and Tomasini, G. (2010). "High-speed train crosswind analysis: CFD study and validation with wind-tunnel tests". *International Conference on Engineering Conferences International*. Potsdam, September. https://doi.org/10.1007/978-3-319-20122-1_6.

Cheli, F., Corradi, R. and Tomasini, G. (2012), "Crosswind action on rail vehicles: A methodology for the estimation of the characteristic wind curves", *Journal of Wind Engineering and Industrial Aerodynamics*. **104** 248-255. https://doi.org/10.1016/j.jweia.2012.04.006.

Cheli, F., Ripamonti, F., Rocchi, D. and Tomasini, G. (2010), "Aerodynamic behaviour investigation of the new EMUV250 train to cross wind", *Journal of Wind Engineering and Industrial Aerodynamics*. **98**(4-5), 189-201. https://doi.org/10.1016/j.jweia.2009.10.015.

Chen, Z., Liu, T., Jiang, Z., Guo, Z. and Zhang, J. (2018), "Comparative analysis of the effect of different nose lengths on train aerodynamic performance under crosswind", *Journal of Fluids and Structures*. **78** 69-85. https://doi.org/10.1016/j.jfluidstructs.2017.12.016.

Chen, Z., Liu, T., Li, W., Guo, Z. and Xia, Y. (2021), "Aerodynamic performance and dynamic behaviors of a train passing through an elongated hillock region beside a windbreak under crosswinds and corresponding flow mitigation measures", *Journal of Wind Engineering and Industrial Aerodynamics*. **208** 104434. https://doi.org/10.1016/j.jweia.2020.104434.

Chen, Z., Liu, T., Yu, M., Chen, G., Chen, M. and Guo, Z. (2020), "Experimental and numerical research on wind characteristics affected by actual mountain ridges and windbreaks: a case study of the Lanzhou-Xinjiang high-speed railway", *Engineering Applications of Computational Fluid Mechanics*. **14**(1), 1385-1403. https://doi.org/10.1080/19942060.2020.1831963.

Chiu, T. and Squire, L. (1992), "An experimental study of the flow over a train in a crosswind at large yaw angles up to 90", *Journal of Wind Engineering and Industrial Aerodynamics*. **45**(1), 47-74. https://doi.org/10.1016/0167-6105(92)90005-U.

Copley, J. (1987), "The three-dimensional flow around railway trains", *Journal of Wind Engineering and Industrial Aerodynamics*. **26**(1), 21-52. https://doi.org/10.1016/0167-6105(87)90034-1.

Davidson, L. (2006). "Evaluation of the SST-SAS model: channel flow, asymmetric diffuser and axi-symmetric hill". *ECCOMAS CFD*. Netherlands, September. http://resolver.tudelft.nl/uuid:5d23e2a6-5675-450d-bf3d-1dd40d736cae.

Gao, H., Liu, T., Gu, H., Jiang, Z., Huo, X., Xia, Y. and Chen, Z. (2021), "Full-scale tests of unsteady aerodynamic loads and pressure distribution on fast trains in crosswinds", *Measurement*. **186** 110152. https://doi.org/10.1016/j.measurement.2021.110152.

García, J., Muñoz-Paniagua, J., Jiménez, A., Migoya, E. and Crespo, A. (2015), "Numerical study of the influence of synthetic turbulent inflow conditions on the aerodynamics of a train", *Journal of Fluids and Structures*. **56** 134-151. https://doi.org/10.1016/j.jfluidstructs.2015.05.002.

Guo, Z., Liu, T., Chen, Z., Liu, Z., Monzer, A. and Sheridan, J. (2020), "Study of the flow around railway embankment of different heights with and without trains", *Journal of Wind Engineering and Industrial*

Aerodynamics. **202** 104203. https://doi.org/10.1016/j.jweia.2020.104203.
Hemida, H. and Krajnović, S. (2009), "Exploring flow structures around a simplified ICE2 train subjected to a 30 side wind using LES", *Engineering applications of computational fluid mechanics*. **3**(1), 28-41. https://doi.org/10.1080/19942060.2009.11015252.
Hemida, H. and Krajnović, S. (2010), "LES study of the influence of the nose shape and yaw angles on flow structures around trains", *Journal of Wind Engineering and Industrial Aerodynamics*. **98**(1), 34-46. https://doi.org/10.1016/j.jweia.2009.08.012.
Huo, X., Liu, T., Yu, M., Chen, Z., Guo, Z., Li, W. and Wang, T. (2020), "Impact of the trailing edge shape of a downstream dummy vehicle on train aerodynamics subjected to crosswind", *Proceedings of the Institution of Mechanical Engineers, Part F: Journal of Rail and Rapid Transit*. 0954409720915039. https://doi.org/10.1177/0954409720915039.
Jiang, Z., Liu, T., Gu, H. and Guo, Z. (2021), "Research on the reasonable end shape of the windbreak wall model in the wind tunnel test via numerical simulation", *Vehicle System Dynamics*. 1-21. https://doi.org/10.1080/00423114.2021.1955136.
Krajnovic, S. (2008). "Numerical simulation of the flow around an ICE2 train under the influence of a wind gust". *2008 International Conference on Railway Engineering-Challenges for Railway Transportation in Information Age*. Hong Kong, March. https://ieeexplore.ieee.org/abstract/document/4730862.
Krajnović, S., Ringqvist, P., Nakade, K. and Basara, B. (2012), "Large eddy simulation of the flow around a simplified train moving through a crosswind flow", *Journal of Wind Engineering and Industrial Aerodynamics*. **110** 86-99. https://doi.org/10.1016/j.jweia.2012.07.001.
Li, T., Qin, D. and Zhang, J. (2019), "Effect of RANS turbulence model on aerodynamic behavior of trains in crosswind", *Chin J Mech Eng-En*. **32**(1), 1-12. https://doi.org/10.1186/s10033-019-0402-2.
Li, W., Liu, T., Martinez-Vazquez, P., Chen, Z., Huo, X., Guo, Z. and Xia, Y. (2021), "Yaw effects on train aerodynamics on a double-track viaduct: A wind tunnel study", *Wind and Structures*. **33**(3), 201-215. https://doi.org/10.12989/was.2021.33.3.201.
Liu, T., Chen, Z., Zhou, X. and Zhang, J. (2018), "A CFD analysis of the aerodynamics of a high-speed train passing through a windbreak transition under crosswind", *Engineering Applications of Computational Fluid Mechanics*. **12**(1), 137-151. https://doi.org/10.1080/19942060.2017.1360211.
Maleki, S., Burton, D. and Thompson, M.C. (2017), "Assessment of various turbulence models (ELES, SAS, URANS and RANS) for predicting the aerodynamics of freight train container wagons", *Journal of Wind Engineering and Industrial Aerodynamics*. **170** 68-80. https://doi.org/10.1016/j.jweia.2017.07.008.
Menter, F. and Egorov, Y. (2010), "The scale-adaptive simulation method for unsteady turbulent flow predictions. Part 1: theory and model description", *Flow, turbulence and combustion*. **85**(1), 113-138. https://doi.org/10.1007/s10494-010-9264-5.
Menter, F. and Kuntz, M. (2004), *Adaptation of eddy-viscosity turbulence models to unsteady separated flow behind vehicles*, Springerhttps://doi.org/10.1007/978-3-540-44419-0_30.
Menter, F.R. (1994), "Two-equation eddy-viscosity turbulence models for engineering applications", *AIAA journal*. **32**(8), 1598-1605. https://doi.org/10.2514/3.12149.
Morden, J.A., Hemida, H. and Baker, C.J. (2015), "Comparison of RANS and detached eddy simulation results to wind-tunnel data for the surface pressures upon a class 43 high-speed train", *Journal of Fluids Engineering*. **137**(4), 041108. https://doi.org/10.1115/1.4029261.
Muñoz-Paniagua, J. and García, J. (2019), "Aerodynamic surrogate-based optimization of the nose shape of a high-speed train for crosswind and passing-by scenarios", *Journal of Wind Engineering and Industrial Aerodynamics*. **184** 139-152. https://doi.org/10.1016/j.jweia.2018.11.014.
Munoz-Paniagua, J., García, J. and Lehugeur, B. (2017), "Evaluation of RANS, SAS and IDDES models for the simulation of the flow around a high-speed train subjected to crosswind", *Journal of Wind Engineering and Industrial Aerodynamics*. **171** 50-66. https://doi.org/10.1016/j.jweia.2017.09.006.
Niu, J.-q., Zhou, D., Liu, T.-h. and Liang, X.-f. (2017), "Numerical simulation of aerodynamic performance of a couple multiple units high-speed train", *Vehicle System Dynamics*. **55**(5), 681-703. https://doi.org/10.1080/00423114.2016.1277769.
Shur, M.L., Spalart, P.R., Strelets, M.K. and Travin, A.K. (2008), "A hybrid RANS-LES approach with

delayed-DES and wall-modelled LES capabilities", *International journal of heat and fluid flow*. **29**(6), 1638-1649. https://doi.org/10.1016/j.ijheatfluidflow.2008.07.001.

Spalart, P. and Shur, M. (1997), "On the sensitization of turbulence models to rotation and curvature", *Aerospace Science and Technology*. **1**(5), 297-302. https://doi.org/10.1016/S1270-9638(97)90051-1.

Spalart, P.R., Deck, S., Shur, M.L., Squires, K.D., Strelets, M.K. and Travin, A. (2006), "A new version of detached-eddy simulation, resistant to ambiguous grid densities", *Theoretical and computational fluid dynamics*. **20**(3), 181-195. https://doi.org/10.1007/s00162-006-0015-0.

Wang, S., Bell, J.R., Burton, D., Herbst, A.H., Sheridan, J. and Thompson, M.C. (2017), "The performance of different turbulence models (URANS, SAS and DES) for predicting high-speed train slipstream", *Journal of Wind Engineering and Industrial Aerodynamics*. **165** 46-57. https://doi.org/10.1016/j.jweia.2017.03.001.

Wang, Y., Xia, H., Guo, W., Zhang, N. and Wang, S. (2018), "Numerical analysis of wind field induced by moving train on HSR bridge subjected to crosswind", *Wind and structures*. **27**(1), 29-40. https://doi.org/10.12989/was.2018.27.1.029.

Zhao, H., Zhai, W. and Chen, Z. (2015), "Effect of noise barrier on aerodynamic performance of high-speed train in crosswind", *Wind and Structures*. **20**(4), 509-525. https://doi.org/10.12989/was.2015.20.4.509.